LED-driven continuous flow carbon dioxide hydrogenation on a nickel-based catalyst

Carlos J. Bueno-Alejo[a,*], Adriana Arca-Ramos[a], Jose L. Hueso[a,b,c], Jesus Santamaria[a,b,c*]

[a]*Institute of Nanoscience of Aragon and Department of Chemical and Environmental Engineering, University of Zaragoza. Campus Río Ebro, Edificio I+D, C/Mariano Esquillor s/n, 50018 Zaragoza (Spain)*

[b]*Networking Research Center on Bioengineering, Biomaterials and Nanomedicine (CIBER-BBN, 28029, Madrid (Spain)*

[c]*Instituto de Ciencia de Materiales de Aragon (ICMA), Consejo Superior de Investigaciones Cientificas (CSIC-Universidad de Zaragoza), 50009, Zaragoza (Spain)*

(*Corresponding Authors´ E-mails: carlosb@unizar.es; Jesus.Santamaria@unizar.es)

ABSTRACT

Methane can be obtained from the direct hydrogenation of CO_2 via the Sabatier reaction. This reaction is usually performed at high temperatures and/or pressures but it has been recently reported that in the presence of certain nanostructured catalysts, CO_2 methanation can proceed at lower temperatures in solar photo-assisted processes. In this study, an inexpensive and commercially available nickel-based catalyst ($Ni/Al_2O_3{\cdot}SiO_2$) has been selected to perform the continuous CO_2 hydrogenation in a fixed bed photocatalytic reactor using high-radiance/low consumption light emitting diodes (LEDs). These illumination conditions allow us to attain the reaction temperatures required without the need of additional heating sources. Different LED excitation wavelengths and irradiances were evaluated. Under selected irradiation

conditions (460 nm wavelength) not only the photothermal but also the photo-catalytic conversion of CO_2 into CH_4 takes place, with high selectivity. Conversion levels above 70% with production rates of ca. 35 mmol $CH_4 \cdot g^{-1} \cdot h^{-1}$ were obtained, outperforming the results obtained by conventional heating methods or with other irradiation wavelengths.

KEYWORDS: Carbon Dioxide Hydrogenation; Methane; Photocatalysis; Photothermal; Nickel catalyst; LED

1. INTRODUCTION

Climate change represents one of the major challenges currently faced by mankind and it has attracted a strong interest within the scientific community in the search for viable and environmentally friendly solutions[1-4]. Carbon dioxide (CO_2) concentration levels in the atmosphere and in the ocean continue to rise and there is a clear need for reducing emissions from industries or transportation[3-5]. A second problem concerns the progressive exhaustion of fossil fuel deposits that will need to be partial or totally replaced by alternative and greener sources. The conversion of CO_2 into renewable fuels or value-added chemicals poses an interesting approach to simultaneously tackle both problems. Thus, heterogeneous catalysis has been used to convert CO_2 into different valuable products such as methane (CH_4), synthesis gas ($CO+H_2$) or methanol (CH_3OH) among others [6-10]. In particular, CH_4 obtained from CO_2 hydrogenation through the Sabatier reaction ($CO_2 + 4H_2 \rightarrow CH_4 + 2H_2O$) has drawn attention in the past years as a way to store energy in chemical bonds [11]. This reaction is usually carried out at moderate to high temperatures (250-400 ºC) and/or pressures (20-70 bar)[12, 13]. As an alternative to the conventional catalytic route, in the last years, several researchers have

proposed the use of photo-thermal and photo-assisted methods to achieve the conversion of CO_2 into methane with production yields approaching but still below the levels required for industrial implementation [14-20]. Ozin and co-workers achieved high conversion of CO_2 using RuO_2 supported in silicon photonic crystal[17]. Scaled-up methane production rates from the micro to the milimolar range (mmol methane per hour and per gram of catalyst) were obtained when illuminating with high intensity (22 suns) simulated solar light due to the high absorption efficiency of the photonic support. This production, though remarkable, was achieved using expensive materials (ruthenium supported on a silicon photonic crystal). In contrast, Garcia and co-workers successfully used more abundant and affordable Ni catalysts to achieve the reduction of CO_2 in a flow reactor, with good methane production rates [15, 16, 19, 20]. In their works, the authors combined conventional heating of the reactor and illumination with a solar simulator lamp in order to perform the photo-assisted reaction. Likewise, the use of other transition metals dispersed in carbon-active[19-22] or lanthanides substrates have been also lately explored in the photoreduction of CO_2[23-25].

In principle, a photothermal strategy is advantageous compared to a conventionally heated reactor because the catalyst surface is directly heated by light, rather than following the conventional heat transfer path, from reactor wall to the reacting fluid to the catalyst. Additionally, an interesting characteristic of photothermal processes relates to the faster heating and cooling of the catalyst in comparison with conventional thermally heated reactors in which both processes are considerably slower. This faster heating may lead to considerable energy savings. , as claimed by Kim et al. [26], who reported a 37% of energy saving during CO_2 hydrogenation using the fast-response energy-efficient photoexcitation of CO_2 adsorbed on metal catalysts.

In this work we have used high power LED emitters that facilitate the input of high photon densities into photoreactors with low energy consumption to perform the hydrogenation of CO_2 into CH_4 and a nickel-based commercial catalyst ($Ni/Al_2O_3{\cdot}SiO_2$). This has allowed us to achieve continuous flow photo-enhanced methane production in the range of mmol of CH_4 produced per hour and per gram of catalyst without the need of any additional heating source thanks to the specific light absorption by our catalysts. An especially relevant photo-response was obtained at an excitation wavelength of 460 nm.

2. EXPERIMENTAL

2.1. Characterization techniques

The absorption spectra were performed in a JASCO V670 spectrophotometer with an integrating sphere module for solids measurements. To determine the crystalline structure and the composition of the particles, with High Angle Annular Dark Field with Scanning Transmission Electron Microscope (HAADF-STEM) and Energy Dispersive X-ray Spectroscopy (EDS) analysis were performed by using a FEI TECNAI F30 and FEI Titan-Cube (80-300 kV) microscopes at an acceleration voltage of 300 kV. To prepare the sample, 10 µL of an ethanolic particle suspension were drop-casted on a Cu holey carbon TEM grid. Powder X-ray diffraction (XRD) analyses were performed in a Rigaku/Max System diffractometer with Cu Kα radiation source (λ = 0.15418 nm). Surface composition was analyzed by X-ray photoelectron spectroscopy (XPS) with an Axis Ultra DLD (Kratos Tech.). The spectra were excited by a monochromatic Al Kα source (1486.6 eV) run at 12 kV and 10 mA and pass energy of 20 eV was used. The binding energies were referenced to the internal C 1s (284.6 eV) standard. Analysis of the peaks was

performed with CasaXPS software, using a weighted sum of Lorentzian and Gaussian component curves after Shirley background subtraction. Temperature programmed reduction (H_2-TPR) was performed using a Quantachrome ChemBET Pulsar TPR/TPD instrument equipped with a thermal conductivity detector (TCD). 50 mg of catalyst were first pre-treated at 115 °C for 1 hour in flowing Ar (70 mL min^{-1}) Reduction was then conducted at a heating rate of 5 °C min^{-1} up to 900 ºC in 5% V:V H_2/Ar with a total flow rate of 20 mL min^{-1}.

2.2. Photocatalytic and catalytic reaction tests

CO_2 hydrogenation tests were carried out in a fixed bed reactor packed on a rectangular-section quartz cell with 45 x 2 x 10 mm dimensions (height x width x length) (Teknokroma) and loaded with 100 mg of commercial Ni/Al_2O_3·SiO_2 catalyst (Sigma Aldrich, with 65% loading of Ni). The gas reactant mixture was fed with mass-flow controllers (Bronkhorst) at 5 mL·min^{-1} with a CO_2:H_2 molar ratio (1:4). The reaction cell was simultaneously illuminated by two high power LEDs (LedEngin) coupled to a custom-designed cooling system used elsewhere [27, 28] and also displayed in Figure 1a. The LEDs were placed at 1 mm distance from the quartz reactor's walls. Different LED excitation wavelengths i.e., 365, 460 and 940 nm, and different light irradiances were explored, ranging from 7 to 2200 mW·cm^{-2} in order to reach the targeted reaction temperature at each specific wavelength. The power was adjusted using a variable power supply (Iso-Tech IPS-405) (with calibration certificate) from RSCAL adjusting the intensity of the LEDs to get the same temperature in all cases. The temperature was also measured with a thermocouple placed in the center of the catalyst bed and after steady state was achieved, the measurements were very stable during reaction.

The experiments carried out under conventional heating conditions (i.e. in the absence of LED illumination) were performed with the aid of a home-made system consisting of an aluminium holder designed to heat the same reactor area as in the quartz reactor used for the photocatalytic test and two heating cartridge connected to an electronic device to control the temperature of the reactor (see Figure 1b). The reaction temperature was monitored in both photo-assisted and conventionally heated reactors with a K-type thermocouple placed at the centre of the catalyst bed (approximate bed dimensions: 10 x 2 x 8 mm). The central position of the thermocouple and the reduced dimensions of the reactor allowed us to compare the results obtained in both modes of operation with minimal temperature deviations. An external thermographic camera that had a direct view of the quartz tube was additionally employed to monitor the temperature in the reaction area (see also Supporting Information, Figure S1). The thermographic camera is a NEC InfRec R300 operating over 8-14 μm and allows temperature measurement between -40 ºC and 500 ºC [28, 29]. On-line reaction products analysis was carried out with the aid of an Agilent 490 Micro GC equipped with a molecular sieve column for H_2, O_2, CO and CH_4 detection, a PPQ column for CO_2 and ethane detection and a 52CB column for oxygenated polar compounds detection (methanol, ethanol, etc…). The action spectra normally used to evaluate the possible different contribution of each wavelength[8] were obtained plotting photonic efficiency versus wavelength. The photonic efficiency (μ) can be defined as [(moles of formed product per second)/(moles of incident photons per second)], where the value of moles of incident photons was calculated for each of the LED wavelengths used in this work.

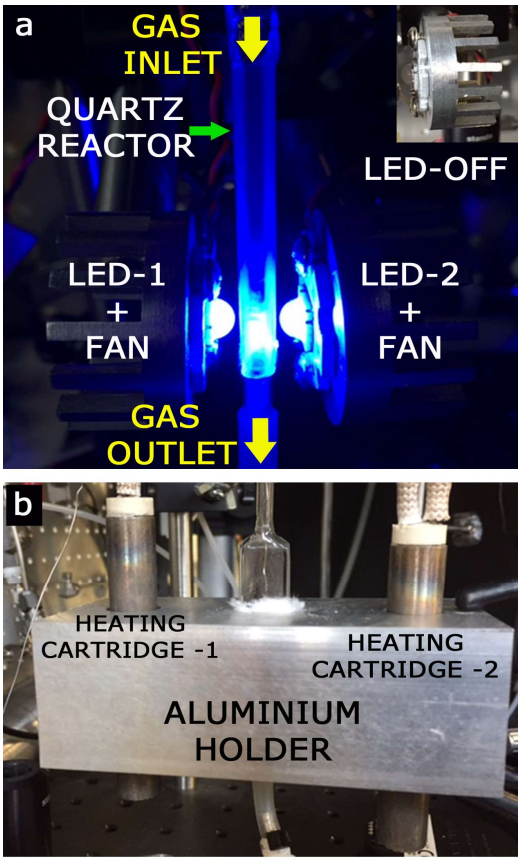

Figure 1. *Digital images of the reactor setup: a) LED illumination system operating alongside the rectangular-shaped quartz reactor in the area where the catalyst bed is placed (inset: detail of the LED and custom-designed cooling fan); b) Custom-made aluminium block designed to house the reactor in the conventional heating experiments with two cylindrical heating cartridges.*

3. RESULTS AND DISCUSSION

3.1. Characterization of the Ni-based catalyst

Figure 2 describes the textural and morpho-chemical characteristics of the commercial Ni-based catalyst employed ($Ni/SiO_2{\cdot}Al_2O_3$) for the LED-driven CO_2 hydrogenation experiments. Keeping in mind that up to 65% wt. Ni was loaded on the silica-alumina support, the combined HAADF-STEM-EDX analyses have revealed different Ni size

distributions that are maintained in both the original (fresh) catalyst and in the used catalyst after multiple reaction cycles (Figure 2). There is a representative fraction of small Ni nanoparticles with average sizes between 6-15 nm that is very homogeneously distributed in the oxide support (Figures 2a-2c-2e-2f and Figure S2 in the Supporting Information). Likewise, there appears a second fraction of bigger entangled nanoparticles with average sizes above 30-50 nm (Figure 2b-Area 2, inset in Figure 2d and Figure 2g) that are mainly composed of a Ni-enriched phase with lower content of oxygen (Figures 2d-2g). The X-ray diffraction data corroborated the co-existence of a cubic phase of metallic Ni and its NiO oxidized counterpart and that both species were present in the catalyst before and after the reaction tests (see Figure 3a). In contrast, high-resolution XPS analysis an increment of Ni in its reduced metallic state after multiple reaction cycles (Figures 3c-3d and Table S1 in the Supporting Information). These results point out to the partial reduction of the catalyst surface when exposed to a hydrogen-rich ambient. It may also indicate the partial removal of adventitious carbon contaminants (i.e. carbonates) initially present on the surface as suggested from surface atomic compositions determined by XPS (see Table S1). H_2-TPR analysis of the catalyst further confirmed the existence of different oxidized Ni species (see Figure S3). The first reduction peak at lower temperatures (T_I=200 ºC) has been ascribed to the presence of Ni^{3+} species and the presence of highly reactive oxygen species readily available for a rapid reduction [30-32]. The second reduction peak with T_{II} ~ 450 ºC has been attributed to the reduction of free NiO nanoparticles with limited interaction with the support [31-35]. Finally, the third reduction region that expands above 580 ºC has been attributed to the reduction of smaller Ni nanoparticles less prone to reducibility due to a stronger interaction metal-support previously reported in the literature and that varies according

the degree of interaction with silica and/or alumina supports [31-41]. The high reduction temperatures account for a very strong interaction and can be probably associated to the smaller nanoparticles readly dispersed in the matrix containing both silica and alumina and high Ni% [42].

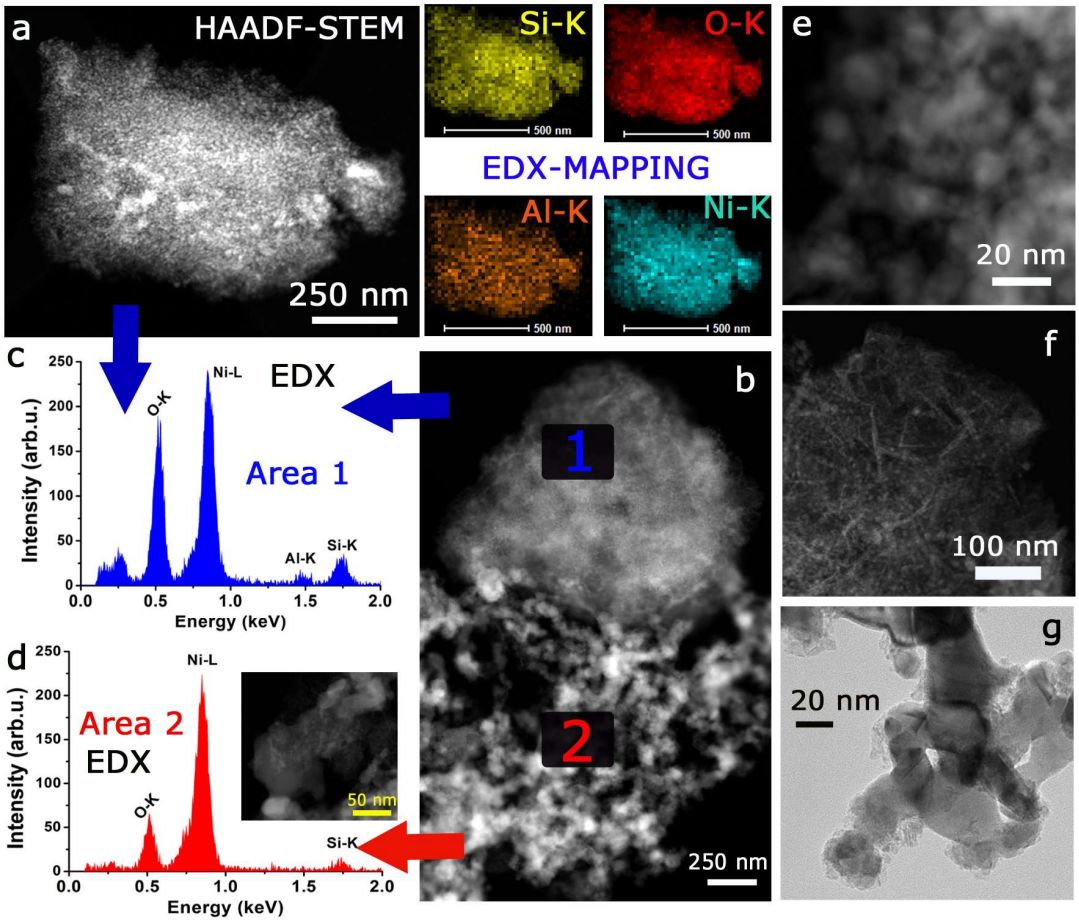

Figure 2. *Characterization of the Ni/SiO_2·Al_2O_3 catalyst by electron microscopy analysis: a) HAADF-STEM image of a representative morphology identified in the catalyst where Ni is very well distributed in the SiO_2-Al_2O_3 oxide matrix as corroborated in the corresponding EDX elemental mapping analysis used to identify the atomic distribution of Si, Al, O and Ni, based on the intensity of their corresponding K-edge transitions; b) HAADF-STEM image displaying the most representative morphologies identified in the*

catalyst before and after reaction; c)-d) EDX spectra corresponding to the areas depicted as 1 and 2 in b, respectively (inset: STEM enlarged image of a bigger Ni nanoparticle representative of the entangled aggregates observed in the area 2 of b); e)-f) STEM images corresponding to smaller Ni nanoparticles; g) TEM image representative of the bigger Ni nanoparticles fraction similar inset d. Please note that similar morphologies and compositions were obtained for both original and spent samples.

The absorption spectrum corresponding to the Ni catalyst shows a broad band in the whole UV-Vis-NIR range (Figure 3b) probably due to the presence of NiO with different particle size [43, 44]. Thus, in principle, it can be considered as a suitable photocatalyst for solar light irradiation, as pointed out by Albero et al.[15] and later by Puga et al. [20]. In their studies, they used a broad spectrum lamp and a few filters in order to evaluate UV and visible light separately. In this work, we have followed a different procedure; evaluating the influence of specific LED irradiation wavelengths and searching for specific contributions to the photo-assisted catalysis (see Figure 3b and highlighted wavelengths).

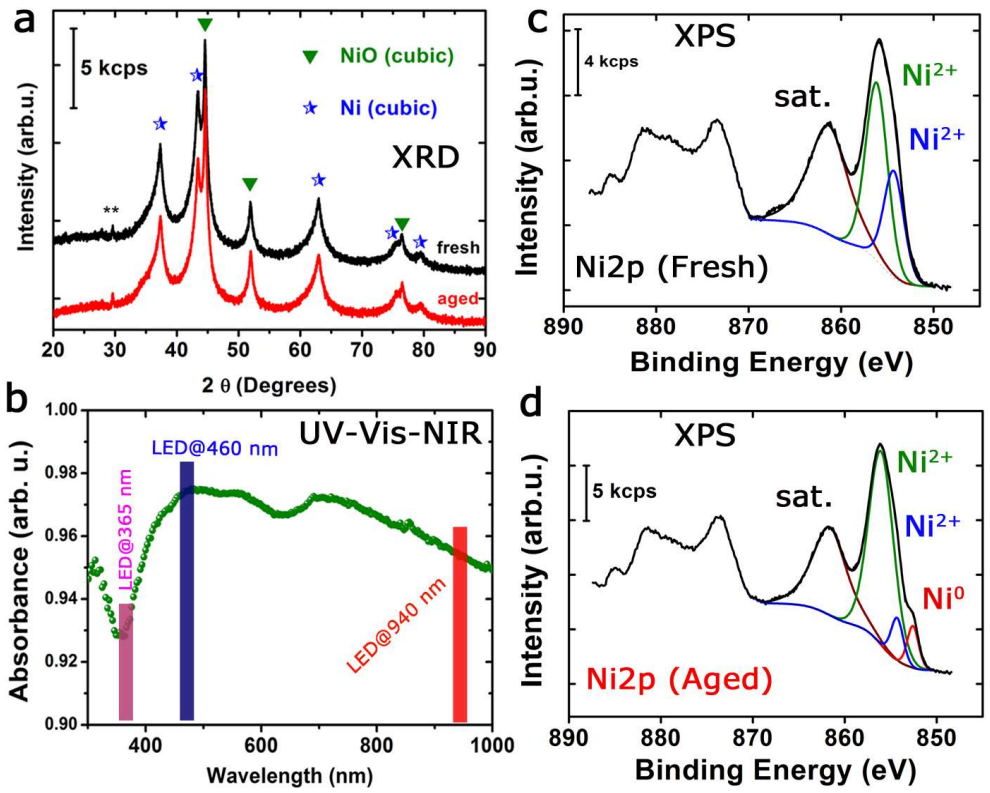

Figure 3. *a) X-ray diffractograms of the catalyst before and after reaction accounting for the presence of cubic phases of Ni in its metallic and oxidized state, the asterisks account for a minimal contribution of the substrate holder; b) UV-Vis-NIR absorption spectrum of the catalyst; the different coloured bars highlight the LED excitation wavelengths selected to perform the photocatalytic experiments; c)-d) X-ray photoemission spectra corresponding to the Ni2p region of the Ni/Al_2O_3•SiO_2 catalyst: fresh and after reaction, respectively; Ni in its reduced state is assigned to a binding energy of 852.6 eV and the typical satellite at 861.5 eV.*

3.2. LED-assisted photocatalytic CO_2 hydrogenation tests

The CO_2 hydrogenation experiments were performed in a photoreactor setup consisting of a quartz reactor with flat walls filled with the desired catalyst and placed between two LED irradiators (Figure 1). Figure 4a shows the CO_2 conversion achieved under

irradiation with UV (λ_{exc} = 365 nm), blue (λ_{exc} = 460 nm) and NIR (λ_{exc} = 940 nm) LEDs modulated at increasing irradiances, respectively. Conventional (thermally heated) reaction experiments at analogous temperatures were also performed to discern purely thermal from photocatalytic effects [15, 20, 21, 24, 45]. These experiments were carried out using the same reactor and catalyst, placed in an aluminium heater made ad-hoc to provide a homogeneous heating for the reactor so that photo- and thermally heated experiments could be reproduced under the same reaction conditions (see results in Figure 4).

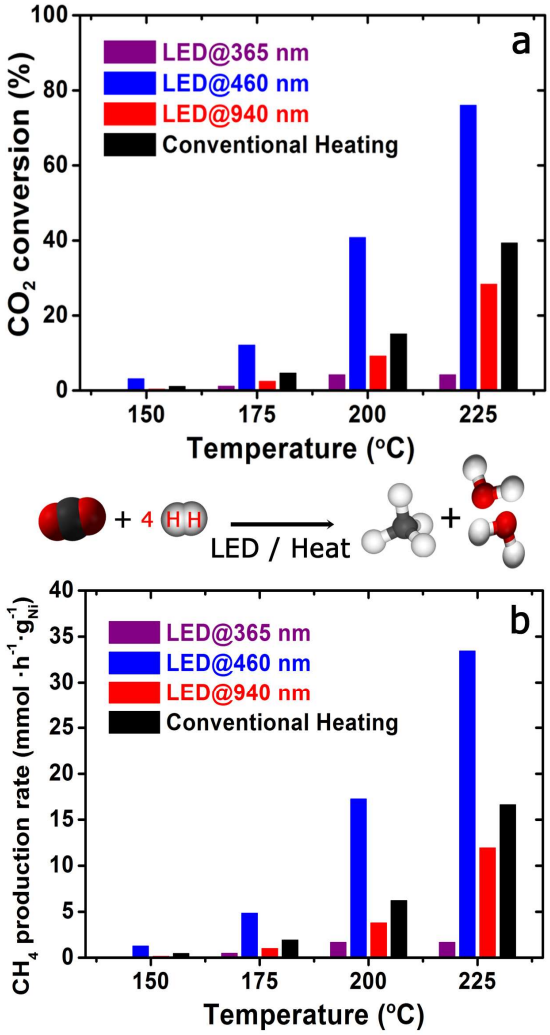

Figure 4. *Evaluation of the performance of the Ni/Al_2O_3·SiO_2 catalyst for the Sabatier reaction at different temperatures achieved under conventional heating (in the absence*

of illumination) and in the absence of external heating under different LED wavelengths (UV-365 nm, Blue-460 nm or NIR-940 nm): a) CO_2 conversion b) Methane production rates; Experimental conditions: CO_2:H_2 (1:4) ratios at 5 mL·min^{-1} feed rate; The selectivity towards CH_4 production (see reaction stoichiometry in the inset) was above 99.5% in all the explored conditions.

CO_2 conversion could be detected at temperatures as low as 150 ^oC for all the wavelengths used as well as under conventional heating conditions (Figure 4a). As the temperature increased, the conversion of CO_2 into methane increased accordingly under all the experimental conditions, although with a very different behaviour. When illuminating with 365 and 940 nm LEDs, lower conversions than in the case of conventional heating were obtained. In these two cases, it seems plausible to attribute the photo-assisted thermal heating of the catalyst to its photonic capabilities rather than . As a result, the Ni-based catalyst is able to efficiently absorb photons almost in the complete UV-Vis-NIR range as previously claimed for different metal based catalysts [20-22] and transform them into heat that activates the Sabatier process thanks to the high selectivity of Ni towards methanation. The absence of a perfectly homogeneous illumination of the catalyst bed reflected an overall lower CO_2 conversion efficiency in contrast to the well-heated conventional heating reactor. The temperature profiles obtained with the thermocouple and the IR camera further confirmed this hypothesis given the radial temperature gradients detected during LED irradiation (see Figure S3). In summary, the average temperature under LED illumination was likely lower than under conventional heating, which explains the lower conversions obtained for every temperature under 365 and 940 nm LED illumination.

Nonetheless, the most remarkable CO_2 methanation results were achieved when illuminating with 460 nm LEDs as shown in Figure 4a. In this case, the CO_2 conversion was roughly doubled at every temperature in comparison with the conventional heating experiment. Likewise, Figure 4b shows similar trends in terms of methane production rates. Maximum production rates of ca. 35 mmol $CH_4 \cdot g^{-1} \cdot h^{-1}$ were obtained under LED@460 nm irradiation which are roughly one order of magnitude higher than previous results in the literature [15, 17] with no significant deactivation after more than 48 h in discontinuous experiments probably due to the work in continuous regime that prevented the accumulation of water [15, 45]. For instance, Ozin and coworkers reported a methanation rate of 4.4 mmol $CH_4 \cdot g^{-1} \cdot h^{-1}$ using RuO_2 supported in silicon photonic crystal. In this case, experiments were performed in a batch reactor and using a high-intensity solar simulator and thanks to the high absorption provided by the photonic crystal, a high photothermal effect could be achieved [17]. Albero et al. used Ni-based catalysts in a continuous flow reactor but with a different configuration and illumination source. In their experiments they pre-heated the reactor to a certain temperature using a hot plate and then illuminated the catalyst with a conventional Xe lamp to perform the photo-assisted reaction. A maximum production rate of 2.7 mmol $CH_4 \cdot g^{-1} \cdot h^{-1}$ was obtained at 225 ^oC [15]. In the present study, the catalyst exhibited an extraordinary performance at 460 nm in comparison with other wavelengths. Since the catalyst has a broad absorption band spanning the visible to infrared ranges, other wavelengths also contribute to catalyst heating, which makes its use promising regarding the use of full-spectrum solar light as green and abundant energy source. This remarkable photo-activation under 460 nm blue light illumination can be in principle attributed to the capability of metallic Ni sites to photo-generate and/or inject electrons

that facilitate the subsequent formation of Ni-H (metal hydrides) as a preliminary step to facilitate the progressive reduction of CO_2 molecules [45-47]. This mechanism is supported by the highly reductive reaction conditions and reducibility observed by TPR at relatively low temperatures (Figure S3). The plasmonic nature of metallic Ni and its localized surface plasmon resonance (LSPR) properties has been previously claimed in the literature as a plausible mechanism to improve the catalytic performance under photo-assisted conditions [10, 20, 21, 45-48]. Initially, the Ni surface is present in an oxidized state that progressively evolves to its metallic state due to the reducing conditions of the reaction (Figure 3d). Even though the surface plasmon resonance of metallic Ni is mostly described in the UV region [49], it has also been assigned to the visible region of the spectrum [50, 51].

Furthermore, Figure 5a shows the action spectrum with the different wavelengths used in this work and a significant enhancement in the photonic efficiency was demonstrated when irradiating with the LED at 460 nm. This photonic efficiency enhancement seems to be indicative not only of a very favourable absorption at that specific wavelength (that would be expected from its absorption spectrum-Figure 3b) but also of the existence of an additional plasmonic phenomenon[8, 47, 48, 52-54]. This additional plasmonic effect may affect the reactions in different ways, but in our case, a second and very likely plasmonic mechanism involving the polarizability of intermediate molecules near the surface of the nanoparticles has been tentatively considered. This effect has been described before for ethylene epoxidation with silver nanoparticles where it has been claimed that this polarization of the molecules favours their adsorption on the surface facilitating further reaction [55]. Another example of this mechanism was reported by

Liu at al. for the CO_2 methanation using gold nanoparticles as plasmonic photocatalyst [23]. In this work the authors were able to activate non-polar bonds in CO_2 and CH_4 by irradiation of hybrid catalyst containing gold nanoparticles. Zhang et al. [22, 56] postulated an analogous polarization of CO_2 by plasmonic iron nanoparticles and its electronic excitation via highly energetic hot electron injection. In contrast, the polarization mechanism would be consistent with the results observed: since it requires the presence of intermediates that can be more easily polarized, a minimum temperature to activate the starting molecules would be required. Previous reports have described the presence of carbonates, formates and carbonyl intermediate species participating in the mechanism of the conversion of CO_2 into methane[57-60]. All of these molecules are more susceptible to be polarized that the starting CO_2 and H_2 molecules.

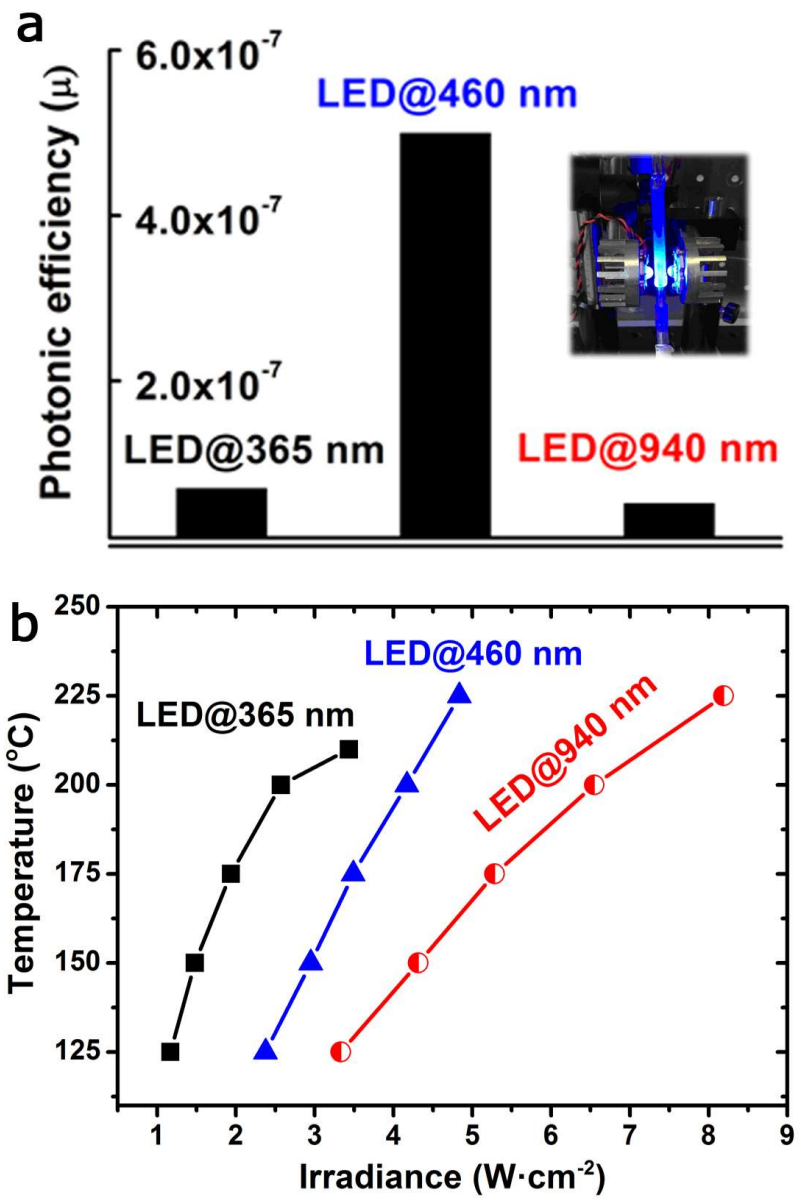

Figure 5. *a) Action spectrum in the form of bar diagram calculated with equation (1) for the three different wavelengths used in this work, 365, 460 and 940 nm. b) Steady state temperatures achieved thanks to the photothermal effect of the different LEDs as a function of irradiances, Inset: Digital photograph of the reactor with the blue-emitting LEDs on.*

It should be noted that, unlike previous reports where broad bands spectrum lamps where used, in this work the LED light power is emitted within a narrow 40 nm range,

so any feature capable of absorbing in that region would absorb more photons, giving rise to an enhanced performance that may explain the strong increase in conversion observed in comparison with previous works[15, 16] where illumination was carried out with a wide spectrum lamp as solar simulator. Furthermore, since in these works a conventional xenon lamp was used at certain distance of the catalyst, the photothermal effect was strongly limited and supplementary conventional heating was necessary. In our case, the high radiance LEDs employed provided sufficient light intensity to heat the catalyst at the reaction temperature, so no external heating was required. Figure 5b shows the influence of progressively increasing LEDs intensity and how the temperature in the catalyst bed reached higher values. Besides, it is worth noting that the increment was different for every LED since the power output of the diodes and the absorption of the solid is different for each wavelength (Figure 5b). Finally, it should be mentioned that using direct catalyst heating by photothermal effects may give rise to a considerable energy saving. Kim et al. estimated this saving to be of 37% in a photo-assisted system compared to a the conventional system[26].

CONCLUSIONS

Nickel-based commercial catalysts can be successfully photo-activated with the aid of high irradiance-low power consumption LEDs to hydrogenate CO_2 into CH_4 with conversions of 76%, selectivities over 99.7% and production rates of up to 35 mmol $CH_4 \cdot g^{-1} \cdot h^{-1}$ at 225ºC. The broad absorption of the Ni catalyst enables its use as a full-range plasmonic photocatalyst that exhibits a combined photocatalytic and photothermal response especially in the range of maximum absorption at 460 nm. Nickel-based nanocatalysts appear as a valid and inexpensive alternative to boost the

light-assisted Sabatier reaction and contribute to the development of greener alternative approaches that can simultaneously tackle greenhouse emissions and hydrocarbon scarcity.

ACKNOWLEDGEMENTS

Financial support from MINECO (Spain) (ARCADIA-CTQ2016-79419-R) and the CIBER-BBN (initiative funded by the VI National R&D&i Plan 2008-2011, Iniciativa Ingenio 2010, Consolider Program, CIBER Actions and financed by the Instituto de Salud Carlos III with assistance from the European Regional Development Fund) is gratefully acknowledged. The microscopy works have been conducted in the "Laboratorio de Microscopias Avanzadas" at "Instituto de Nanociencia de Aragon - Universidad de Zaragoza. Dr. Irusta is fully acknowledged for performing the XPS analysis. A.A.R. thanks the Spanish Government for a Juan de la Cierva postdoctoral fellowship.

References

[1] R.J. Lim, M.S. Xie, M.A. Sk, J.M. Lee, A. Fisher, X. Wang, K.H. Lim, Catalysis Today 233 (2014) 169-180.

[2] K. Li, X. An, K.H. Park, M. Khraisheh, J. Tang, Catalysis Today 224 (2014) 3-12.

[3] P. Lanzafame, S. Perathoner, G. Centi, S. Gross, E.J.M. Hensen, Catal. Sci. Technol. 7 (2017) 5182-5194.

[4] S. Perathoner, S. Gross, E.J.M. Hensen, H. Wessel, H. Chraye, G. Centi, ChemCatChem 9 (2017) 904-909.

[5] R.K. Pachauri, L. Meyer, IPCC, 2014: Climate Change 2014: Synthesis Report. Contribution of Working Groups I, II and III to the Fifth Assessment Report of the Intergovernmental Panel on Climate Change, 2014 ed., The Intercontinental Panel for Climate Change, IPCC, Geneva, Switzerland, 2015, p. 151.

[6] G.W. Zhan, H.C. Zeng, Acs Catalysis 7 (2017) 7509-7519.

[7] C.S. Chen, C.S. Budi, H.C. Wu, D. Saikia, H.M. Kao, Acs Catalysis 7 (2017) 8367-8381.

[8] H. Robatjazi, H. Zhao, D.F. Swearer, N.J. Hogan, L. Zhou, A. Alabastri, M.J. McClain, P. Nordlander, N.J. Halas, Nature Communications 8 (2017) 27.

[9] J. Jia, H. Wang, Z.L. Lu, P.G. O'Brien, M. Ghoussoub, P. Duchesne, Z.Q. Zheng, P.C. Li, Q. Qiao, L. Wang, A. Gu, A.A. Jelle, Y.C. Dong, Q. Wang, K.K. Ghuman, T. Wood, C.X. Qian, Y. Shao, C.Y. Qiu, M.M. Ye, Y.M. Zhu, Z.H. Lu, P. Zhang, A.S. Helmy, C.V. Singh, N.P. Kherani, D.D. Perovic, G.A. Ozin, Advanced Science 4 (2017) 13.

[10] S. Jantarang, E.C. Lovell, T.H. Tan, J. Scott, R. Amal, Prog. Nat. Sci. 28 (2018) 168-177.

[11] S. Rönsch, J. Schneider, S. Matthischke, M. Schlüter, M. Götz, J. Lefebvre, P. Prabhakaran, S. Bajohr, Fuel 166 (2016) 276-296.

[12] J.J. Gao, Y.L. Wang, Y. Ping, D.C. Hu, G.W. Xu, F.N. Gu, F.B. Su, Rsc Advances 2 (2012) 2358-2368.

[13] J. Kopyscinski, T.J. Schildhauer, S.M.A. Biollaz, Fuel 89 (2010) 1763-1783.

[14] G.A. Ozin, Advanced Materials 27 (2015) 1957-1963.

[15] J. Albero, E. Dominguez, A. Corma, H. Garcia, Sustainable Energy & Fuels 1 (2017) 1303-1307.

[16] F. Sastre, A.V. Puga, L. Liu, A. Corma, H. García, Journal of the American Chemical Society 136 (2014) 6798-6801.

[17] A.A. Jelle, K.K. Ghuman, P.G. O'Brien, M. Hmadeh, A. Sandhel, D.D. Perovic, C.V. Singh, C.A. Mims, G.A. Ozin, Advanced Energy Materials 8 (2018) 1702277.

[18] X. Meng, T. Wang, L. Liu, S. Ouyang, P. Li, H. Hu, T. Kako, H. Iwai, A. Tanaka, J. Ye, Angewandte Chemie 126 (2014) 11662-11666.

[19] A.V. Puga, Top. Catal. 59 (2016) 1268-1278.

[20] A.V. Puga, A. Corma, Top. Catal. 61 (2018) 1810-1819.

[21] L.C. Liu, A.V. Puga, J. Cored, P. Concepcion, V. Perez-Dieste, H. Garcia, A. Corma, Appl. Catal. B-Environ. 235 (2018) 186-196.

[22] H.B. Zhang, T. Wang, J.J. Wang, H.M. Liu, T.D. Dao, M. Li, G.G. Liu, X.G. Meng, K. Chang, L. Shi, T. Nagao, J.H. Ye, Advanced Materials 28 (2016) 3703-3710.

[23] H.M. Liu, X.G. Meng, T.D. Dao, H.B. Zhang, P. Li, K. Chang, T. Wang, M. Li, T. Nagao, J.H. Ye, Angew. Chem.-Int. Edit. 54 (2015) 11545-11549.

[24] X. Zhang, X. Li, M.E. Reish, D. Zhang, N.Q. Su, Y. Gutiérrez, F. Moreno, W. Yang, H.O. Everitt, J. Liu, Nano Letters (2018).

[25] X. Zhang, X. Li, D. Zhang, N.Q. Su, W. Yang, H.O. Everitt, J. Liu, Nature Communications 8 (2017) 14542.

[26] C. Kim, S. Hyeon, J. Lee, W.D. Kim, D.C. Lee, J. Kim, H. Lee, Nature Communications 9 (2018).

[27] J. Graus, C.J. Bueno-Alejo, J.L. Hueso, Catalysts 8 (2018) 16.

[28] C.J. Bueno-Alejo, J.L. Hueso, R. Mallada, I. Julian, J. Santamaria, Chem. Eng. J. 358 (2019) 1363-1370.

[29] A. Ramirez, J.L. Hueso, M. Abian, M.U. Alzueta, R. Mallada, J. Santamaria, Sci. Adv. 5 (2019).

[30] B. Mile, D. Stirling, M.A. Zammitt, A. Lovell, M. Webb, Journal of Molecular Catalysis 62 (1990) 179-198.

[31] A.P. Grosvenor, M.C. Biesinger, R.S. Smart, N.S. McIntyre, Surf. Sci. 600 (2006) 1771-1779.

[32] S. Mahammadunnisa, P.M.K. Reddy, N. Lingaiah, C. Subrahmanyam, Catal. Sci. Technol. 3 (2013) 730-736.

[33] C.P. Li, Y.W. Chen, Thermochim. Acta 256 (1995) 457-465.

[34] W.X. Zou, C.Y. Ge, M.Y. Lu, S.G. Wu, Y.Z. Wang, J.F. Sun, Y. Pu, C.J. Tang, F. Gao, L. Dong, RSC Advances 5 (2015) 98335-98343.

[35] S.R. Kirumakki, B.G. Shpeizer, G.V. Sagar, K.V.R. Chary, A. Clearfield, J. Catal. 242 (2006) 319-331.

[36] J.T. Richardson, B. Turk, M. Lei, K. Forster, M.V. Twigg, Appl. Catal. A-Gen. 83 (1992) 87-101.

[37] L.F. Zhang, J.F. Lin, Y. Chen, J. Chem. Soc.-Faraday Trans. 88 (1992) 2075-2078.

[38] V.L. Barrio, P.L. Arias, J.F. Cambra, M.B. Guemez, J.M. Campos-Martin, B. Pawelec, J.L.G. Fierro, Appl. Catal. A-Gen. 248 (2003) 211-225.

[39] C. Guimon, A. Auroux, E. Romero, A. Monzon, Appl. Catal. A-Gen. 251 (2003) 199-214.

[40] G. Poncelet, M.A. Centeno, R. Molina, Appl. Catal. A-Gen. 288 (2005) 232-242.

[41] V.V. Kaichev, A.Y. Gladky, I.P. Prosvirin, A.A. Saraev, M. Havecker, A. Knop-Gericke, R. Schlogl, V.I. Bukhtiyarov, Surf. Sci. 609 (2013) 113-118.

[42] R. Wang, Y.H. Li, R.H. Shi, M.M. Yang, J. Mol. Catal. A-Chem. 344 (2011) 122-127.

[43] V.I. Sokolov, A.V. Druzhinin, G.A. Kim, N.B. Gruzdev, A.Y. Yermakov, M.A. Uimin, I.V. Byzov, N.N. Shchegoleva, V.B. Vykhodets, T.E. Kurennykh, Physica B 430 (2013) 1-5.

[44] A. Rostamnejadi, S. Bagheri, Appl. Phys. A-Mater. Sci. Process. 123 (2017) 9.

[45] J. Albero, H. Garcia, A. Corma, Top. Catal. 59 (2016) 787-791.

[46] D. Mateo, J. Albero, H. Garcia, Appl. Catal. B-Environ. 224 (2018) 563-571.

[47] J. Ren, H.L. Guo, J.Z. Yang, Z.F. Qin, J.Y. Lin, Z. Li, Appl. Surf. Sci. 351 (2015) 504-516.

[48] J.N.G. Stanley, I. Garcia-Garcia, T. Perfrement, E.C. Lovell, T.W. Schmidt, J. Scott, R. Amal, Chem. Eng. Sci. 194 (2019) 94-104.

[49] S. Schuermans, T. Maurer, J. Martin, J.B. Moussy, J. Plain, Opt. Mater. Express 7 (2017) 1787-1793.

[50] J. Chen, P. Albella, Z. Pirzadeh, P. Alonso - González, F. Huth, S. Bonetti, V. Bonanni, J. Åkerman, J. Nogués, P. Vavassori, A. Dmitriev, J. Aizpurua, R. Hillenbrand, Small 7 (2011) 2341-2347.

[51] Z. Pirzadeh, T. Pakizeh, V. Miljkovic, C. Langhammer, A. Dmitriev, ACS Photonics 1 (2014) 158-162.

[52] K.C. Kao, Y. Kuroiwa, H. Nishi, T. Tatsuma, Phys. Chem. Chem. Phys. 19 (2017) 31429-31435.

[53] S. Sarina, E. Jaatinen, Q. Xiao, Y.M. Huang, P. Christopher, J.C. Zhao, H.Y. Zhu, J. Phys. Chem. Lett. 8 (2017) 2526-2534.

[54] S.K. Lee, A. Mills, C. O'Rourke, Chemical Society Reviews 46 (2017) 4877-4894.

[55] X.Z. Liang, P. Wang, M.M. Li, Q.Q. Zhang, Z.Y. Wang, Y. Dai, X.Y. Zhang, Y.Y. Liu, M.H. Whangbo, B.B. Huang, Appl. Catal. B-Environ. 220 (2018) 356-361.

[56] X. Zhang, X.Q. Li, M.E. Reish, D. Zhang, N.Q. Su, Y. Gutierrez, F. Moreno, W.T. Yang, H.O. Everitt, J. Liu, Nano Letters 18 (2018) 1714-1723.

[57] C. Vogt, E. Groeneveld, G. Kamsma, M. Nachtegaal, L. Lu, C.J. Kiely, P.H. Berben, F. Meirer, B.M. Weckhuysen, Nature Catalysis 1 (2018) 127-134.

[58] S. Saeidi, S. Najari, F. Fazlollahi, M.K. Nikoo, F. Sefidkon, J.J. Klemes, L.L. Baxter, Renew. Sust. Energ. Rev. 80 (2017) 1292-1311.

[59] Y. Kohno, T. Tanaka, T. Funabiki, S. Yoshida, Phys. Chem. Chem. Phys. 2 (2000) 2635-2639.
[60] X. Wang, H. Shi, J. Szanyi, Nature Communications 8 (2017) 6.

SUPPORTING INFORMATION

LED-driven continuous flow carbon dioxide hydrogenation on a nickel-based catalyst

Carlos J. Bueno-Alejo[a,*], Adriana Arca-Ramos[a], Jose L. Hueso[a,b,c], Jesus Santamaria[a,b,c*]

[a]*Institute of Nanoscience of Aragon and Department of Chemical and Environmental Engineering, University of Zaragoza. Campus Río Ebro, Edificio I+D, C/Mariano Esquillor s/n, 50018 Zaragoza (Spain)*

[b]*Networking Research Center on Bioengineering, Biomaterials and Nanomedicine (CIBER-BBN, 28029, Madrid (Spain)*

[c]*Instituto de Ciencia de Materiales de Aragon (ICMA), Consejo Superior de Investigaciones Cientificas (CSIC-Universidad de Zaragoza), 50009, Zaragoza (Spain)*

(*Corresponding Authors´ E-mails: carlosb@unizar.es ; Jesus.Santamaria@unizar.es)

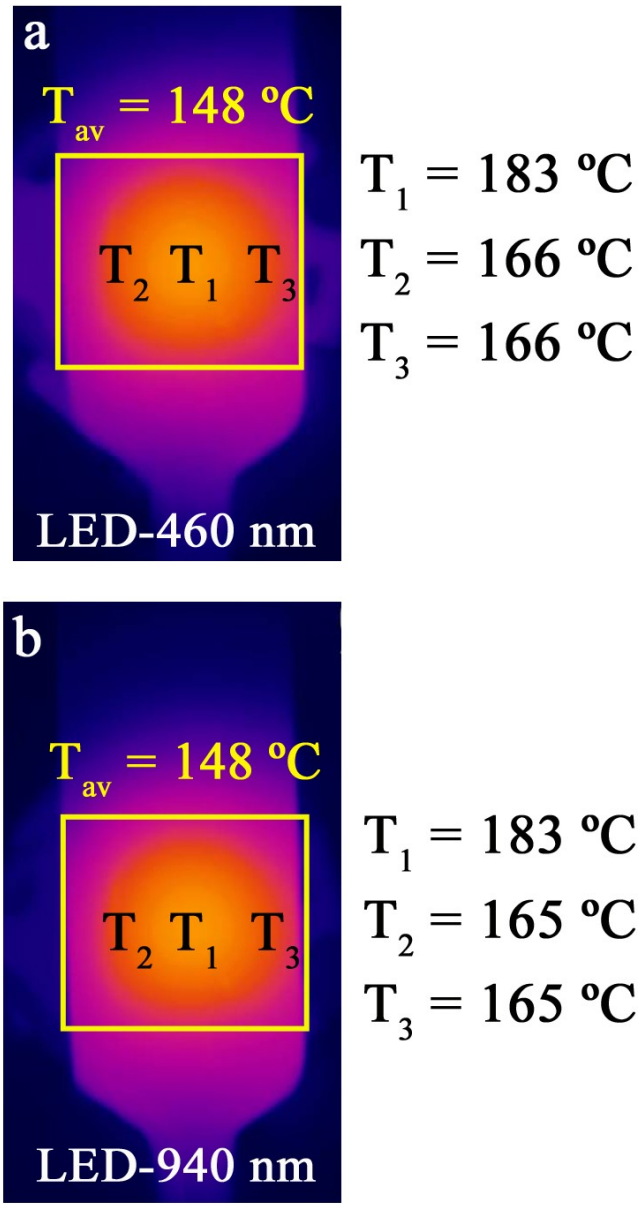

Figure S1: *Thermal images of the front-side quartz reactor acquired during the irradiation of the catalyst bed with: a) LED irradiating at 460 nm; b) LED irradiating at 940 nm, respectively. The mapping of temperatures and individual selected temperature readings within the hotter zone of the reactor reveal a very similar temperature distribution with a radial decay from the center to the sides in accordance to the illumination pattern of the LEDs. The temperatures measured with a thermocouple placed at the center of the catalytic beds were close to 200 ºC in all cases.*

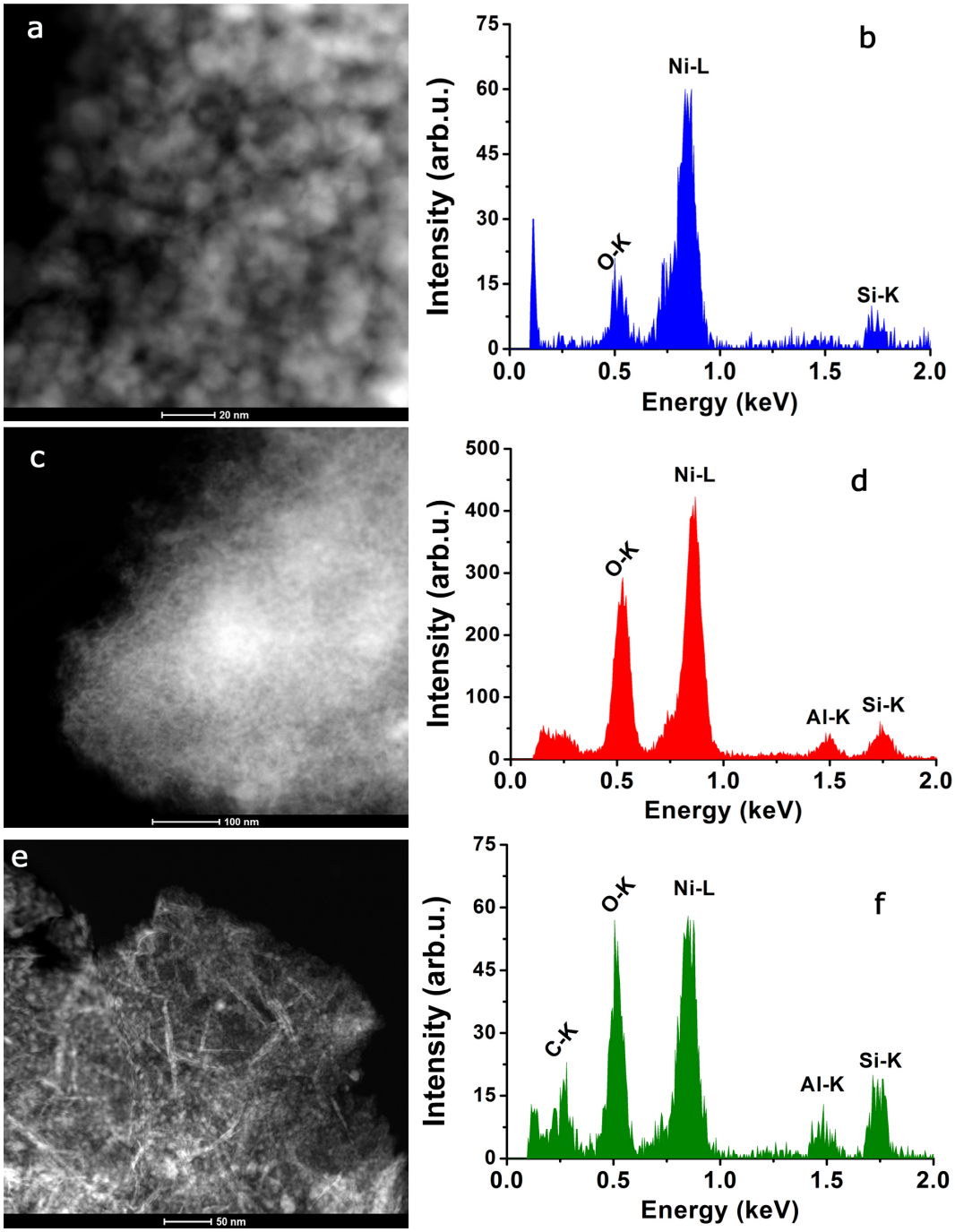

Figure S2. *Additional HAADF-STEM images and EDX analysis of representative morphologies observed in the Ni/Al_2O_3·SiO_2 catalyst.*

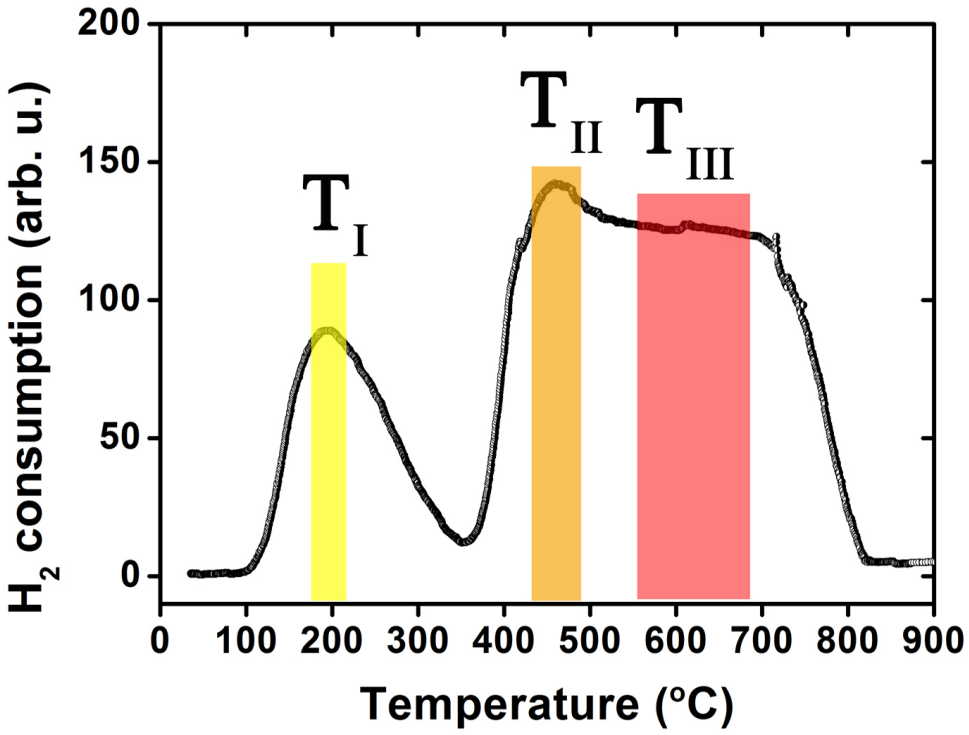

Figure S3: *Temperature Programmed Reduction of the Ni-based catalyst (Ar:H_2 (5% v/v, 5ºC/min, total flow 20 mL/min, 50 mg_{cat})*

Table S1. Atomic surface composition identified by XPS analysis

Sample	B.E. (eV) Atomic %				
	Ni 2p	O 1s	C 1s	Si 2p	Al 2p
Fresh	856.0 25.5%	531.6 53.6%	285.0 14.2%	102.4 5.6%	74.6 1.1%
Aged	856.1 26.7%	531.6 56.0%	285.0 10.6%	102.6 6.7%	74.1 0.7%